

From Physical Degradation Models to Task-Aware All-in-One Image Restoration

Hu Gao¹ Xiaoning Lei² Xichen Xu¹ Xingjian Wang³ Lizhuang Ma¹

Abstract

All-in-one image restoration aims to adaptively handle multiple restoration tasks with a single trained model. Although existing methods achieve promising results by introducing prompt information or leveraging large models, the added learning modules increase system complexity and hinder real-time applicability. In this paper, we adopt a physical degradation modeling perspective and predict a task-aware inverse degradation operator for efficient all-in-one image restoration. The framework consists of two stages. In the first stage, the predicted inverse operator produces an initial restored image together with an uncertainty perception map that highlights regions difficult to reconstruct, ensuring restoration reliability. In the second stage, the restoration is further refined under the guidance of this uncertainty map. The same inverse operator prediction network is used in both stages, with task-aware parameters introduced after operator prediction to adapt to different degradation tasks. Moreover, by accelerating the convolution of the inverse operator, the proposed method achieves efficient all-in-one image restoration. The resulting tightly integrated architecture, termed OPIR, is extensively validated through experiments, demonstrating superior all-in-one restoration performance while remaining highly competitive on task-aligned restoration.

1. Introduction

Image restoration (IR) aims to recover a latent clean image J from an observed degraded image I . The degradation process is generally formulated as:

$$I = \mathcal{D}_t(J) \quad (1)$$

where $\mathcal{D}_t(\cdot)$ denotes a task-dependent degradation operator and t is the degradation type. The restoration objective

¹Shanghai Jiao Tong University, Shanghai, China ²CATL, Ningde, China ³Beijing Normal University, Beijing, China. Correspondence to: Lizhuang Ma <lzma@sjtu.edu.cn>.

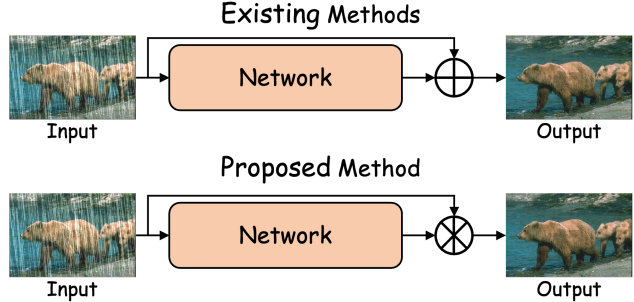


Figure 1. Mechanisms of existing methods vs. our method.

is to estimate J from I under unknown and task-specific degradation mechanisms. IR is inherently ill-posed, as a single degraded image may correspond to multiple plausible solutions. Traditional methods (He et al., 2011; Rong et al., 2024) tackle this by introducing task-specific priors, modeling the degradation process, and applying inverse operations. While effective in some cases, they depend heavily on strong assumptions about degradation factors. In real-world scenarios, where degradations are often uncertain or unknown, accurate modeling becomes challenging, leading to limited generalization and unstable performance.

Deep learning methods (Su et al., 2025; Cui et al., 2023a; Zeng et al., 2025) have significantly advanced IR by learning the statistical properties of natural images, enabling them to implicitly capture a wide range of priors and often outperform traditional approaches. According to how many degradation types a single model can accommodate, existing IR methods can be broadly divided into three categories: task-specific, task-aligned, and all-in-one. Task-specific approaches (Su et al., 2025; Guo et al., 2025b) focus on individual restoration tasks by designing specialized models that are optimized for particular degradation characteristics. Task-aligned methods (Cui et al., 2023a; Gu et al., 2025) pursue a more general framework by sequentially training a single network on datasets with different degradations, enabling it to support multiple restoration tasks. In contrast, all-in-one methods (Potlapalli et al., 2023; Zeng et al., 2025) train a unified model on mixed degradation types simultaneously, allowing one network to flexibly address a variety of restoration tasks.

Although existing all-in-one IR methods have demonstrated

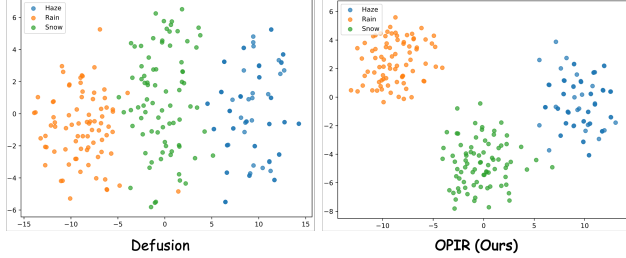


Figure 2. The figure shows t-SNE visualizations of degradation embeddings from OPIR (our method) and Defusion (Luo et al., 2025), with our model displaying more distinct and well-separated clusters.

strong performance through the design of prompts or the adoption of large-scale models, the introduction of additional learning modules inevitably increases system complexity and limits their practicality in real-time applications. This observation motivates us to explore a more efficient alternative by learning task-aware inverse degradation operators directly from the degradation modeling process, aiming to achieve effective all-in-one IR while maintaining computational efficiency. As shown in Figure 1, existing methods predict the residual image from the degraded input using deep learning models and obtain the final restored image by adding this residual to the degraded image. In contrast, our method predicts the inverse degradation operator and produces the restored image by convolving it with the degraded input. By accelerating this convolution process, efficient IR is achieved.

Specifically, our framework follows a two-stage design. In the first stage, the predicted inverse degradation operator produces an initial restored image along with an uncertainty perception map, which highlights regions that are difficult to reconstruct and ensures restoration reliability. In the second stage, this uncertainty map guides further refinement, enabling more precise recovery in challenging areas. The same inverse operator prediction network is used in both stages, with task-aware parameters introduced after operator prediction to adapt effectively to different degradation tasks. As shown in Figure 2, OPIR generates more distinct clusters, indicating a stronger ability to differentiate degradation types. Extensive experiments further demonstrate that our method achieves state-of-the-art performance in both all-in-one and task-aligned IR.

The main contributions of this work are:

1. We propose OPIR for all-in-one image restoration, taking a physical degradation modeling approach and predicting a task-aware inverse degradation operator to achieve efficient restoration. Extensive experiments demonstrate its superior performance in both all-in-one and task-aligned IR.

2. We design a two-stage framework where the predicted inverse degradation operator first generates an initial restored image with an uncertainty map to ensure reliability, and then this map guides further refinement for more accurate recovery in challenging regions.
3. We design a task-aware inverse operator with adaptive parameters for different degradation tasks, which can be efficiently implemented via convolution accelerated

2. Related Works

2.1. Image Restoration

Image restoration (IR) aims to recover high-quality images from degraded inputs, a challenging and inherently ill-posed problem. Traditional approaches (He et al., 2011; Rong et al., 2024) tackle this by introducing handcrafted priors to constrain the solution space. However, these priors rely heavily on expert knowledge and often exhibit limited adaptability, resulting in poor generalization across diverse degradation scenarios.

With the rapid development of deep learning in vision tasks, numerous data-driven IR methods (Gao et al., 2024c; Mao et al., 2024; Cui et al., 2023a; Gu et al., 2025; Zeng et al., 2025) have been proposed, leveraging statistical regularities of natural images to implicitly learn priors and surpass traditional methods. Depending on how many degradation types a single model can handle, these methods are broadly classified into task-specific, task-aligned, and all-in-one approaches.

Task-specific methods (Su et al., 2025; Guo et al., 2025b) design dedicated models for individual degradations, often customized to the target dataset. ALGNet (Gao et al., 2024a) introduces local feature extraction to reduce pixel forgetting for precise deblurring, XYScanNet (Liu et al., 2025) uses alternating intra- and inter-slice scanning to capture spatial dependencies, and EfDeRain+ (Guo et al., 2025b) formulates deraining as predictive filtering, avoiding complex rain modeling. Diffusion-based approaches, such as UPID-EDM (Wen et al., 2024), leverage vision-language priors to remove degradations while preserving structure, while PGH²Net (Su et al., 2025) combines bright/dark channel priors with histogram equalization for hierarchical dehazing. Diff-Unmix (Zeng et al., 2024) achieves self-supervised denoising through spectral decomposition and conditional diffusion.

Task-aligned methods (Cui et al., 2023a; Gu et al., 2025) aim to build general networks capable of handling multiple degradations by sequential training across diverse datasets. MambaIR (Guo et al., 2024) and MambaIRV2 (Guo et al., 2025a) introduce multi-directional unfolding and non-causal modeling to enhance spatial and state-space representations.

SFNet (Cui et al., 2023d) and FSNet (Cui et al., 2023a) employ dynamic frequency selection to focus on the most informative components, while ACL (Gu et al., 2025) exploits the equivalence between linear attention and state-space models to unlock linear attention for restoration. MHNNet (Gao et al., 2025) adopts a mixed hierarchical design to generate restorations with richer textures and finer structural details.

All-in-one methods (Potlapalli et al., 2023; Zeng et al., 2025) extend this concept further, training a single network to handle multiple degradation types simultaneously. PromptIR (Potlapalli et al., 2023) uses lightweight prompt modules for direct restoration, CAPTNet (Gao et al., 2024b) leverages data-component changes through prompt learning, and NDR (Yao et al., 2024) captures shared degradation characteristics via neural representations. Large models further enhance all-in-one IR. VLU-Net (Zeng et al., 2025) uses vision-language features to automatically identify degradation-aware keys, AutoDIR (Jiang et al., 2024) combines VLM guidance with latent diffusion for structure-consistent restoration, AdaIR (Cui et al., 2025) separates degradation from content across spatial and frequency domains, and Defusion (Luo et al., 2025) applies visual instruction-guided degradation diffusion. PerceiveIR (Zhang et al., 2025) introduces a two-stage design that identifies both degradation types and fine-grained severity levels, achieving strong transferability across restoration tasks. Although existing all-in-one IR methods achieve strong performance using prompts or large-scale models, added learning modules increase system complexity and limit real-time applicability. In this paper, we take a physical degradation modeling approach and predict a task-aware inverse degradation operator for efficient all-in-one image restoration.

2.2. Kernel-Predicted Restoration

Kernel-predicted techniques have been widely used in image restoration due to the local coherence, continuity, and structural properties of natural images. Traditional methods rely on handcrafted kernels and priors to process images locally, including adaptive (Awate & Whitaker, 2006), recursive (Kundur & Hatzinakos, 1998), bilateral (Zhang & Gunturk, 2008), and collaborative 3-D transform-domain approaches (Dabov et al., 2007). While effective in certain cases, these methods often struggle with complex degradations such as rain streaks, where bilateral kernels may blur the image and guided kernels can introduce artifacts. With the rise of deep learning, predictive kernel methods have emerged as a powerful alternative. Kernel Prediction Networks (KPN) (Mildenhall et al., 2018) learn per-pixel, image-adaptive kernels through deep convolutional networks, enabling flexible, data-driven restoration. These approaches have been successfully applied to various image restoration tasks (Guo et al., 2025c; 2021; Fu et al.,

2021). However, most existing methods overlook multi-scale modeling, and the effectiveness of the predicted kernels is seldom explicitly evaluated, which can result in distorted details. To alleviate this issue, EfDeRain+ (Guo et al., 2025b) introduces a weight-sharing multi-scale dilated filtering strategy, but it remains task-specific and cannot accommodate multiple restoration tasks within a unified framework. To overcome these limitations, we propose a task-aware kernel prediction framework that incorporates multi-scale uncertainty modeling and task-aware parameters, enabling efficient all-in-one image restoration.

3. Method

3.1. Problem Definition

As shown in Eq. 1, the restoration objective is to estimate J from I under unknown and task-specific degradation mechanisms. The modeling of degradation varies across different restoration tasks. Deraining is typically modeled as an additive process:

$$I = J + \sum_{k=1}^K R_k \quad (2)$$

where R_k denotes individual rain streak components. Desnowing explicitly accounts for occlusion effects through a masking mechanism:

$$I = M \odot S + (1 - M) \odot J \quad (3)$$

where M represents the snow mask and S denotes snow particles. Dehazing follows the atmospheric scattering model:

$$I(x) = J(x), t(x) + A(1 - t(x)) \quad (4)$$

where $t(x)$ is the transmission map and A denotes the global atmospheric light. Despite their different formulations, these degradation models can be unified as:

$$I = H_t J + b_t \quad (5)$$

where H_t represents a task-dependent degradation operator and b_t denotes a bias term. Under this unified view, deraining, desnowing, and dehazing can all be interpreted as inverse problems with unknown degradation operators.

Although the degradation operators differ across tasks, their corresponding bias terms are often strongly correlated. Therefore, we adopt a joint prediction strategy. Instead of explicitly estimating H_t and b_t , we directly learn a task-aware inverse mapping:

$$\hat{J} = \mathcal{G}(I; \theta_t) \quad (6)$$

where $\mathcal{G}(\cdot)$ denotes a shared restoration backbone modulated by task-aware parameters θ_t . From an operator-learning perspective, the model learns a family of inverse operators

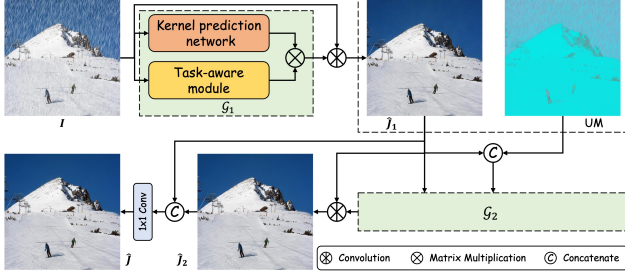


Figure 3. The overall architecture of the proposed OPIR is composed of two stages.

$\mathcal{G}_t \approx \mathcal{D}_t^{-1}$. Accordingly, image restoration can be formulated as the following optimization problem:

$$\min ||\mathcal{G}(I; \theta_t) - J|| \quad (7)$$

To further enhance restoration performance, as shown in Figure 3, we design a two-stage strategy. In the first stage, the model predicts not only the inverse mapping but also an uncertainty estimation map. In the second stage, this uncertainty map is leveraged to focus on severely degraded regions, enabling an all-in-one restoration framework across diverse degradation types. Accordingly, Eq. (6) can be rewritten as:

$$\hat{J} = \mathcal{G}_2(\mathcal{G}_1(I; \theta_{t1}); \theta_{t2}) \quad (8)$$

In this paper, our objective is to learn $\mathcal{G}_1(\cdot)$ and $\mathcal{G}_2(\cdot)$. The functions $\mathcal{G}_1(\cdot)$ and $\mathcal{G}_2(\cdot)$ share the same network architecture and are defined as:

$$\begin{aligned} \mathcal{G}_1(I; \theta_t) &= \text{TAIOM}(I) \\ &= (\text{KPN}(I) \otimes \text{TAM}(I)) \odot I \end{aligned} \quad (9)$$

where TAIOM denotes the task-aware inverse operator modeling. Here, KPN refers to the kernel prediction network implemented with a U-Net (Chen et al., 2022) architecture, and TAM represents the task-aware module.

3.2. Task-Aware Inverse Operator Modeling

Different restoration tasks correspond to distinct physical degradation processes, requiring specialized inverse operators. Rather than learning independent operators for each task, we introduce a task-aware modulation mechanism to adapt a shared predicted operator. Specifically, a lightweight task-aware module $\mathcal{T}(\cdot)$ modulates the base operator using task-specific parameters θ_t :

$$\tilde{K} = \mathcal{T}(K; \theta_t) = \text{KPN}(I) \otimes \text{TAM}(I) \quad (10)$$

where $\text{KPN}(\cdot)$ denotes the kernel prediction network and $\text{TAM}(\cdot)$ the task-aware module. This design allows a single backbone to predict operators while maintaining task-specific adaptability with minimal overhead.

To improve restoration reliability, we estimate per-pixel reconstruction uncertainty from the predicted operator. For pixel p , the uncertainty score is computed as the mean absolute value of kernel weights in its local neighborhood $\mathcal{N}(p)$:

$$UM(p) = \frac{1}{k^2} \sum_{q \in \mathcal{N}(p)} |K_p(q)| \quad (11)$$

yielding an uncertainty map $UM \in \mathbb{R}^{H \times W}$ that highlights regions difficult to reconstruct and serves as guidance in the refinement stage. Based on this formulation, we adopt a two-stage inverse operator modeling strategy. In the first stage, the task-aware operator produces an initial restoration \hat{J}_1 along with the uncertainty map:

$$\hat{J}_1 = \tilde{K}_1 \odot I \quad (12)$$

In the second stage, the same network refines the restoration conditioned on the intermediate result and uncertainty map:

$$\begin{aligned} \hat{J}_2 &= \tilde{K}_2 \odot \hat{J}_1, \\ \tilde{K}_2 &= \mathcal{T}(K_2; \theta_{t2}) = \text{KPN}(\hat{J}_1 \odot UM) \otimes \text{TAM}(\hat{J}_1) \end{aligned} \quad (13)$$

By explicitly modeling task-awareness and uncertainty-guided refinement, the proposed TAIOM captures degradation-specific characteristics while generalizing across diverse tasks.

Furthermore, for degradations that span large regions, a small receptive field may fail to capture sufficient clean context, whereas larger kernels can leverage distant pixels to enhance reconstruction quality. This observation naturally motivates a multi-scale filtering formulation. Following (Guo et al., 2025b), we employ a multi-scale filtering strategy that decouples kernel size from kernel parameters, significantly reducing computational complexity. To recover a clean image \hat{J} from an observed degraded image $I \in \mathbb{R}^{H \times W \times C}$, instead of predicting separate kernels $K^{(s)}$ for each scale s , we define a single shared base kernel and reuse it across multiple scales via dilation:

$$K \in \mathbb{R}^{H \times W \times 3 \times 3} \quad (14)$$

$$K_p^{(s)}(\Delta) = K_p(\delta), \quad \Delta = s \cdot \delta, \quad \delta \in \{-1, 0, 1\}^2 \quad (15)$$

where positions not covered by this mapping are set to zero. The output at scale s for pixel p is:

$$\hat{J}^{(s)}(p) = \sum_{\delta \in \{-1, 0, 1\}^2} K_p(\delta) \cdot I(p + s\delta) \quad (16)$$

Table 1. Quantitative results in the all-in-one setting with task-specific, task-aligned, and all-in-one IR methods.

Type	Methods	Deraining		Desnowing		Dehazing		Average	
		PSNR \uparrow	SSIM \uparrow						
Specific	MSP-Former (Chen et al., 2023)	29.25	0.906	32.81	0.955	32.89	0.970	31.65	0.944
	EfDeRain+ (Guo et al., 2025b)	31.18	0.912	29.96	0.938	33.25	0.971	31.46	0.940
	PGH ² Net (Su et al., 2025)	29.89	0.907	32.18	0.943	35.55	0.983	32.21	0.944
	ALGNet (Gao et al., 2024a)	29.32	0.905	31.56	0.944	33.11	0.977	31.33	0.942
Aligned	FSNet (Cui et al., 2023a)	30.85	0.909	32.88	0.947	34.82	0.981	32.85	0.946
	MHNet (Gao et al., 2025)	30.69	0.906	32.03	0.943	34.59	0.980	32.44	0.943
	PPTformer (Wang et al., 2025)	30.88	0.910	32.80	0.945	34.66	0.980	32.78	0.945
	ACL (Gu et al., 2025)	31.11	0.912	32.91	0.948	34.81	0.981	32.94	0.947
All-in-One	AdaIR (Cui et al., 2025)	31.22	0.911	32.99	0.949	35.31	0.982	33.17	0.947
	VLU-Net (Zeng et al., 2025)	31.07	0.910	33.02	0.952	35.43	0.984	33.17	0.949
	Perceive-IR (Zhang et al., 2025)	31.13	0.911	33.11	0.952	35.35	0.983	33.20	0.949
	Defusion (Luo et al., 2025)	30.98	0.910	33.29	0.953	35.52	0.985	33.26	0.949
	OPIR(Ours)	31.96	0.914	34.14	0.959	35.96	0.984	34.02	0.952

To further reduce computation, we note that kernel weights are shared across scales. Let $\Delta_s = \{s \cdot \delta \mid \delta \in \{-1, 0, 1\}^2\}$ denote sampled offsets, and $I_{\text{sampled}} \in \mathbb{R}^{H \times W \times 9 \times S}$ the tensor of sampled image values for S scales. Then the multi-scale convolution can be written as:

$$\hat{J}_p^{(s)} = \sum_{i=1}^9 K_p(\delta_i) \cdot I_{\text{sampled}}(p, i, s) \quad (17)$$

reducing per-pixel complexity from $\mathcal{O}(HW(2s+1)^2)$ to $\mathcal{O}(9HW)$, independent of S , and avoiding explicit materialization of $K^{(s)}$. Finally, we adopt a learnable fusion $\alpha_p^{(s)}$ across scales:

$$\hat{I}_p = \sum_{s=1}^S \alpha_p^{(s)} \cdot \hat{J}_p^{(s)}, \quad \sum_{s=1}^S \alpha_p^{(s)} = 1, \quad \alpha_p^{(s)} \geq 0 \quad (18)$$

This approach enables adaptive selection of the effective receptive field per pixel while maintaining low computational footprint. Compared to (Guo et al., 2025b), our method generates all scale offsets in a single loop, performs multi-scale convolution in parallel, and compresses redundant computation with learnable fusion weights.

3.3. Task-Aware Module

Different image restoration tasks correspond to distinct degradation processes, requiring task-specific adaptation of the predicted inverse operator. To achieve this efficiently, we introduce a task-aware module (TAM) that modulates a shared base kernel K using lightweight, task-specific parameters θ_t . The TAM also facilitates spatially-varying modulation to emphasize different regions depending on the task. Let p index a pixel and $\mathcal{N}(p)$ its local neighborhood. Then the modulated kernel for pixel p is:

$$\tilde{K}_p(q) = K_p(q) \cdot m_p(q; \theta_t), \quad q \in \mathcal{N}(p), \quad (19)$$

where $m_p(q; \theta_t)$ is the task-aware modulation weight predicted by TAM. The restored pixel is then obtained via local convolution:

$$\hat{J}_p = \sum_{q \in \mathcal{N}(p)} \tilde{K}_p(q) \cdot I(q). \quad (20)$$

To jointly handle multiple tasks, we introduce a vector of task embeddings $\mathbf{e}_t \in \mathbb{R}^d$, and define the TAM output as a function of both the local kernel and the task embedding:

$$m_p(q; \theta_t) = g_{\text{TAM}}(K_p(q), \mathbf{e}_t), \quad (21)$$

where $g_{\text{TAM}}(\cdot)$ is implemented as a lightweight MLP. This design allows the operator to adapt dynamically to the degradation type while maintaining a shared backbone, reducing memory and computation overhead compared to learning independent kernels for each task.

4. Experiments

In this section, we first describe the experimental setup, followed by qualitative and quantitative comparison results. Finally, we present ablation studies to validate the effectiveness of our approach. **Due to page limits, more experiments we show in the appendix B.**

4.1. Experimental Setup

We conducted experiments under both the all-in-one and task-aligned settings. **Owing to page limitations, detailed information about the datasets and training procedures is provided in Appendix B1.**

Datasets. For the task-aligned setting, we train the deraining model using 13,712 paired clean-rain images collected from multiple datasets (Yang et al., 2016; Zhang et al., 2017; Fu et al., 2017; Li et al., 2016). The trained OPIR is evaluated

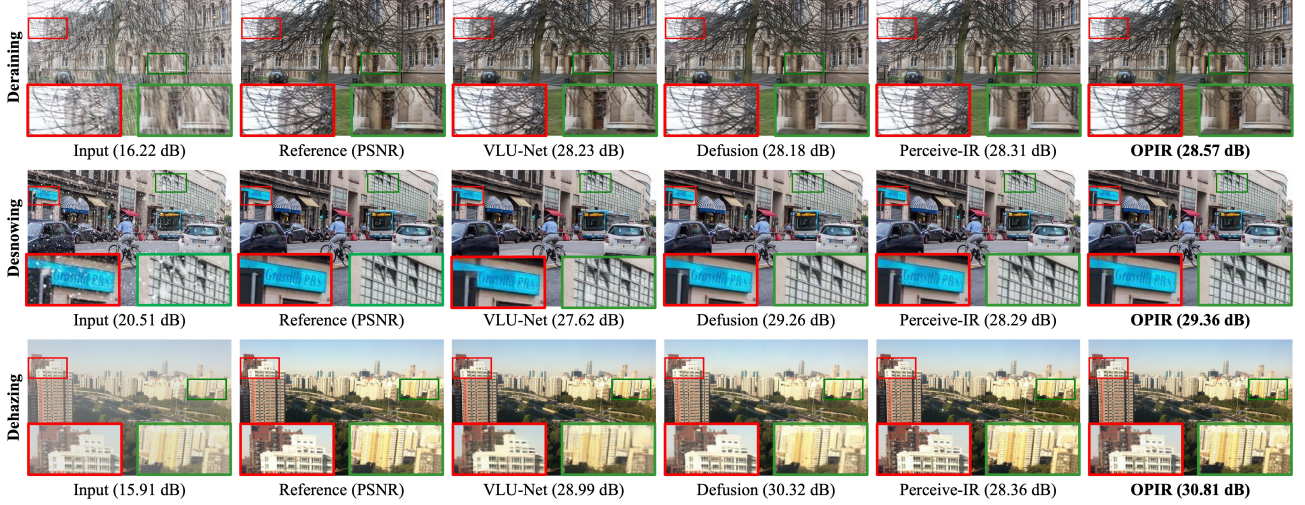


Figure 4. Qualitative results under the all-in-one experimental setup. Our OPIR recovers finer details in the reconstructed images.

on several benchmark test sets, including Rain100H (Yang et al., 2016), Rain100L (Yang et al., 2016), Test100 (Zhang et al., 2017), and Test1200 (Zhang & Patel, 2018). For desnowing evaluation, we adopt the Snow100K (Liu et al., 2018), SRSS (Chen et al., 2020), and CSD (Chen et al., 2021) datasets. For dehazing, we assess the performance of our OPIR on daytime synthetic datasets from RESIDE (Li et al., 2018), which include the indoor training set (ITS), the outdoor training set (OTS), and the synthetic objective testing set (SOTS). For the all-in-one setting, we combine the above image restoration datasets to construct a training set. During evaluation, we use Test100 (Zhang et al., 2017) for deraining, Snow100K (Liu et al., 2018) for desnowing, and SOTS-Outdoor (Li et al., 2018) for dehazing.

4.2. Experimental Results

4.2.1. ALL-IN-ONE SETTING

Table 1 provides a comprehensive comparison among task-specific, task-aligned, and all-in-one image restoration methods under the all-in-one evaluation setting. The results clearly demonstrate the effectiveness and practical value of the proposed OPIR in terms of performance gains and robustness across diverse restoration tasks.

Compared with task-specific methods, OPIR exhibits significantly better generalization. Although task-specific approaches such as PGH²Net (Su et al., 2025) and EfDeRain+ (Guo et al., 2025b) achieve strong performance on their respective target degradations, their performance degrades noticeably on other tasks, resulting in limited average scores. In contrast, OPIR surpasses the best task-specific method by +1.81 dB in average PSNR demonstrating.

Compared with task-aligned methods, which are trained sequentially across different datasets, OPIR consistently

achieves higher accuracy. For example, OPIR improves upon the strongest task-aligned baseline ACL (Gu et al., 2025) by +1.08 dB in average PSNR. This indicates that explicit task-aware operator modeling is more effective than sequential alignment in capturing the intrinsic differences among degradation types.

Compared with state-of-the-art all-in-one methods, OPIR still delivers clear and consistent improvements. Specifically, OPIR outperforms Defusion (Luo et al., 2025), the strongest competing all-in-one baseline, by +0.76 dB in average PSNR. Moreover, OPIR achieves the best PSNR on all three tasks, +0.74 dB over the best baseline on deraining, +0.85 dB on desnowing, and +0.44 dB on dehazing. These consistent gains across tasks highlight the advantage of modeling task-aware inverse degradation operators over prompt-based or diffusion-based designs. As shown in Figure 4, our model produces restored images that are sharper and visually closer to the ground truth than others.

4.2.2. TASK-ALIGNED SETTING

To demonstrate that the proposed OPIR is effective not only for all-in-one restoration but also for task-specific scenarios, we conduct experiments on three representative image restoration tasks: image deraining, image denoising, and image dehazing.

Image Deraining. Following the protocol in prior work (Gao et al., 2025), we evaluate PSNR and SSIM metrics on the Y channel of the YCbCr color space for the image deraining task. Table 2 reports the quantitative results of image deraining under the task-aligned setting. Our proposed OPIR consistently outperforms all compared methods across most datasets. Specifically, on Test100 (Zhang et al., 2017) and Test1200 (Jiang et al., 2020), OPIR achieves

Table 2. Image deraining results in the task-aligned setting.

Methods	Test100		Test1200		Rain100H		Rain100L		Average	
	PSNR ↑	SSIM ↑								
FSNet (Cui et al., 2023a)	31.05	0.919	33.08	0.916	31.77	0.906	38.00	0.972	33.48	0.928
MHNNet (Gao et al., 2025)	31.25	0.901	<u>33.45</u>	0.925	31.08	0.899	<u>40.04</u>	<u>0.985</u>	33.96	0.928
PPTformer (Wang et al., 2025)	31.48	<u>0.922</u>	33.39	0.911	31.77	0.907	39.33	0.983	33.99	0.931
ACL (Gu et al., 2025)	<u>31.51</u>	0.914	33.27	<u>0.928</u>	32.22	<u>0.920</u>	39.18	0.983	34.05	<u>0.936</u>
EfDeRain+ (Guo et al., 2025b)	31.10	0.911	33.12	0.925	34.57	0.957	39.03	0.972	<u>34.46</u>	0.941
OPIR(Ours)	33.15	0.923	35.19	0.941	<u>32.38</u>	0.913	41.01	0.986	35.43	0.941

Table 3. Image desnowing results in the task-aligned setting.

Methods	CSD		SRRS		Snow100K	
	PSNR ↑	SSIM ↑	PSNR ↑	SSIM ↑	PSNR ↑	SSIM ↑
NAFNet (Chen et al., 2022)	33.13	0.96	29.72	0.94	32.41	<u>0.95</u>
FocalNet (Cui et al., 2023b)	37.18	0.99	31.34	0.98	33.53	<u>0.95</u>
MSP-Former (Chen et al., 2023)	33.75	0.96	30.76	<u>0.95</u>	33.43	0.96
IRNeXt (Cui et al., 2023c)	<u>37.29</u>	0.99	<u>31.91</u>	0.98	33.61	<u>0.95</u>
PEUNet (Guo et al., 2025d)	37.28	0.97	31.89	0.98	<u>34.11</u>	0.96
OPIR(Ours)	37.74	0.98	33.10	0.98	34.58	0.96

33.15 dB and 35.19 dB in PSNR, respectively, surpassing previous state-of-the-art methods by a clear margin. On Rain100L (Yang et al., 2016), OPIR reaches 41.01 dB PSNR, demonstrating superior capability in handling light rain conditions. Although EfDeRain+ (Guo et al., 2025b) attains the highest scores on Rain100H (Yang et al., 2016), our method still maintains competitive performance while achieving the best average PSNR (35.43 dB) and SSIM (0.941) across all datasets. These results indicate that OPIR not only effectively restores diverse rain streak patterns but also provides stable and robust performance in various deraining scenarios. Figure 5 illustrates that the images restored by our OPIR effectively reduce color distortion compared to other state-of-the-art methods. Moreover, our approach is able to reconstruct finer and sharper details in the degraded regions.

Image Desnowing. Table 3 presents quantitative comparisons of image desnowing performance on three benchmark datasets: CSD, SRRS, and Snow100K. Our proposed OPIR consistently achieves the highest PSNR across all datasets, with 37.74 dB on CSD, 33.10 dB on SRRS, and 34.58 dB on Snow100K. In particular, OPIR achieves a 0.45 dB improvement on the CSD dataset (Chen et al., 2021), an impressive 2.07 dB gain on the SRRS dataset (Chen et al., 2020) and a 0.97 dB improvement on the Snow100K dataset (Liu et al., 2018) when compared with IRNeXt (Cui et al., 2023c). These results highlight the model’s superior capability in handling diverse snow patterns and background complexities. Furthermore, relative to MSP-Former (Chen et al., 2023), a task-specific architecture tailored for image desnowing, OPIR exhibits substantial quantitative gains of 1.15 dB, 2.34 dB, and 3.99 dB on the Snow100K, SRRS, and CSD datasets, respectively. This demonstrates that our adaptive multi-degradation design not only generalizes effectively to snow removal tasks but also achieves state-of-

Table 4. Image dehazing results in the task-aligned setting.

Methods	SOTS-Indoor		SOTS-Outdoor	
	PSNR ↑	SSIM ↑	PSNR ↑	SSIM ↑
SFNet (Cui et al., 2023d)	41.24	0.996	<u>40.05</u>	0.996
IRXNext (Cui et al., 2023c)	41.21	<u>0.996</u>	39.18	0.996
DEA-Net-CR (Chen et al., 2024)	41.31	0.995	36.59	0.990
Defusion (Luo et al., 2025)	41.65	0.995	37.41	0.993
PGH ² Net (Su et al., 2025)	41.70	0.996	37.52	0.989
OPIR(Ours)	42.21	0.997	40.54	0.990

the-art restoration quality across different data distributions. These results demonstrate that OPIR not only excels in desnowing across multiple datasets but also provides robust and reliable performance.

Image Dehazing. Table 4 reports quantitative comparisons on the SOTS (Li et al., 2018) benchmark for image dehazing. OPIR consistently outperforms all competing methods on both the SOTS-Indoor and SOTS-Outdoor subsets. On SOTS-Indoor, OPIR achieves a PSNR of 42.21 dB, surpassing the previous best method, PGH²Net (Su et al., 2025), by 0.51 dB. On the more challenging SOTS-Outdoor dataset, OPIR attains 40.54 dB PSNR, exceeding the strongest baseline SFNet (Cui et al., 2023d) by 0.49 dB, while maintaining comparable SSIM performance. These consistent improvements demonstrate that OPIR more effectively removes haze while preserving fine structures and visual fidelity, highlighting its robustness and strong generalization capability across both indoor and outdoor dehazing scenarios.

4.3. Ablation Studies

We perform ablation studies under the all-in-one setting and conduct a step-by-step analysis by progressively incorporating the proposed modules to validate the effectiveness of each component, as summarized in Table 5.

Starting from a single-stage baseline without any proposed modules (a), the model achieves a PSNR of 32.31 dB. By introducing the task-aware module alone (b), the PSNR increases by 0.95 dB, indicating that explicitly conditioning the restoration process on task-specific information significantly improves performance. Incorporating the multi-scale kernel prediction module (c) yields a gain of 0.64 dB, demonstrating the effectiveness of multi-scale modeling.

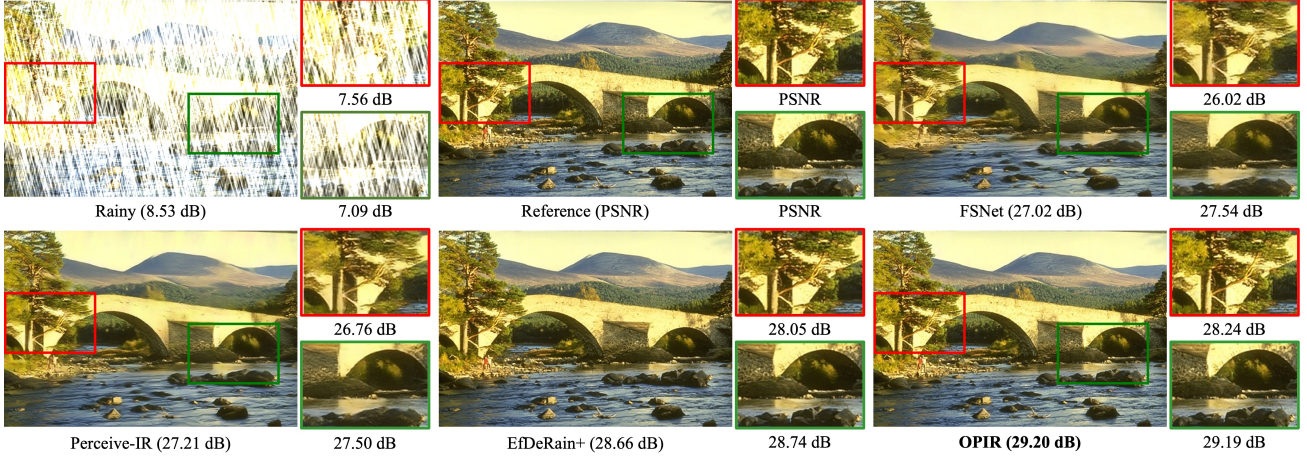


Figure 5. Qualitative results under the task-aligned experimental setup. Our OPIR is able to reconstruct finer and sharper details.

Table 5. Ablation study on individual components of OPIR.

Method	Stage	Uncertainty map	Task-aware module	Multi-scale kernel	PSNR	Δ PSNR
(a)	1				32.31	-
(b)	1		✓		33.26	+ 0.95 dB
(c)	1			✓	32.95	+ 0.64 dB
(d)	1		✓	✓	33.52	+ 1.21 dB
(e)	2		✓	✓	33.77	+ 1.46 dB
(f)	2	✓	✓	✓	34.02	+ 1.71 dB

Table 6. The evaluation of model computational complexity.

Method	Time(s)	Flops(G)	PSNR
VLU-Net (Zeng et al., 2025)	0.743	143	33.17
PromptIR (Potlapalli et al., 2023)	1.012	134	33.04
Perceive-IR (Zhang et al., 2025)	0.682	144	33.20
OPIR(Ours)	0.174	47	34.02

When both the task-aware module and multi-scale kernel prediction are jointly applied within a single stage (d), the PSNR further improves to 33.52 dB, achieving a cumulative gain of 1.21 dB over the baseline. This result suggests that these two components are complementary, where task awareness guides the kernel prediction process to better adapt to different restoration tasks.

We further extend the model to a two-stage architecture (e), which leads to an additional improvement of 0.25 dB compared to its single-stage counterpart, highlighting the benefit of progressive refinement in image restoration. Finally, by integrating the uncertainty map into the two-stage model (f), OPIR reaches the best performance of 34.02 dB, corresponding to a total gain of 1.71 dB over the baseline. This improvement verifies that uncertainty-aware modeling effectively captures spatially varying degradation confidence, enabling more robust kernel prediction and restoration.

4.4. Resource Efficient

We further analyze the computational efficiency of OPIR by comparing its runtime and FLOPs with recent state-of-the-art methods. As shown in Table 6, OPIR not only achieves leading restoration performance but also significantly reduces computational demand. In particular, it surpasses the previous best method, Perceive-IR (Zhang et al., 2025), by 0.82 dB while requiring only 25.5% of its inference time.

5. Conclusion

We propose OPIR, an efficient all-in-one image restoration framework based on physical degradation modeling. By predicting a task-aware inverse degradation operator, OPIR avoids the need for additional prompt modules or large-scale models, significantly reducing system complexity while retaining strong practical efficiency. The proposed two-stage architecture first generates an initial restoration along with an uncertainty perception map to identify challenging regions, and then refines the results under the guidance of this uncertainty information. A shared inverse operator prediction network and task-aware parameters enable effective adaptation to diverse degradation types, while convolution-based operator implementation ensures computational efficiency. Extensive experimental results demonstrate that OPIR achieves superior performance.

References

Awate, S. and Whitaker, R. Unsupervised, information-theoretic, adaptive image filtering for image restoration. *IEEE Transactions on Pattern Analysis and Machine Intelligence*, 28(3):364–376, 2006.

Chen, L., Chu, X., Zhang, X., and Sun, J. Simple baselines for image restoration. *ECCV*, 2022.

Chen, S., Ye, T., Liu, Y., Liao, T., Jiang, J., Chen, E., and Chen, P. Msp-former: Multi-scale projection transformer for single image desnowing. In *ICASSP 2023 - 2023 IEEE International Conference on Acoustics, Speech and Signal Processing (ICASSP)*, pp. 1–5, 2023. doi: 10.1109/ICASSP49357.2023.10095605.

Chen, W.-T., Fang, H.-Y., Ding, J.-J., Tsai, C.-C., and Kuo, S.-Y. Jstasr: Joint size and transparency-aware snow removal algorithm based on modified partial convolution and veiling effect removal. In *Computer Vision–ECCV 2020: 16th European Conference, Glasgow, UK, August 23–28, 2020, Proceedings, Part XXI 16*, pp. 754–770. Springer, 2020.

Chen, W.-T., Fang, H.-Y., Hsieh, C.-L., Tsai, C.-C., Chen, I., Ding, J.-J., Kuo, S.-Y., et al. All snow removed: Single image desnowing algorithm using hierarchical dual-tree complex wavelet representation and contradict channel loss. In *Proceedings of the IEEE/CVF International Conference on Computer Vision*, pp. 4196–4205, 2021.

Chen, Z., He, Z., and Lu, Z.-M. Dea-net: Single image dehazing based on detail-enhanced convolution and content-guided attention. *IEEE Transactions on Image Processing*, 2024.

Cui, Y., Ren, W., Cao, X., and Knoll, A. Image restoration via frequency selection. *TPAMI*, pp. 1–16, 2023a.

Cui, Y., Ren, W., Cao, X., and Knoll, A. Focal network for image restoration. In *Proceedings of the IEEE/CVF International Conference on Computer Vision*, pp. 13001–13011, 2023b.

Cui, Y., Ren, W., Yang, S., Cao, X., and Knoll, A. Irnext: Rethinking convolutional network design for image restoration. In *Proceedings of the 40th International Conference on Machine Learning*, 2023c.

Cui, Y., Tao, Y., Bing, Z., Ren, W., Gao, X., Cao, X., Huang, K., and Knoll, A. Selective frequency network for image restoration. In *ICLR*, 2023d.

Cui, Y., Zamir, S. W., Khan, S., Knoll, A., Shah, M., and Khan, F. S. AdaIR: Adaptive all-in-one image restoration via frequency mining and modulation. In *The Thirteenth International Conference on Learning Representations*, 2025.

Dabov, K., Foi, A., Katkovnik, V., and Egiazarian, K. Image denoising by sparse 3-d transform-domain collaborative filtering. *IEEE Transactions on Image Processing*, 16(8): 2080–2095, 2007.

Fu, L., Zhou, C., Guo, Q., Juefei-Xu, F., Yu, H., Feng, W., Liu, Y., and Wang, S. Auto-exposure fusion for single-image shadow removal. In *2021 IEEE/CVF Conference on Computer Vision and Pattern Recognition (CVPR)*, pp. 10566–10575, 2021.

Fu, X., Huang, J., Zeng, D., Huang, Y., Ding, X., and Paisley, J. Removing rain from single images via a deep detail network. In *2017 IEEE Conference on Computer Vision and Pattern Recognition (CVPR)*, pp. 1715–1723, 2017. doi: 10.1109/CVPR.2017.186.

Gao, H., Ma, B., Zhang, Y., Yang, J., Yang, J., and Dang, D. Learning enriched features via selective state spaces model for efficient image deblurring. In *Proceedings of the 32nd ACM International Conference on Multimedia*, pp. 710–718, 2024a.

Gao, H., Yang, J., Zhang, Y., Wang, N., Yang, J., and Dang, D. Prompt-based ingredient-oriented all-in-one image restoration. *IEEE Transactions on Circuits and Systems for Video Technology*, 34(10):9458–9471, 2024b.

Gao, H., Yang, J., Zhang, Y., Yang, J., Ma, B., and Dang, D. Learning optimal combination patterns for lightweight stereo image super-resolution. In *Proceedings of the 32nd ACM International Conference on Multimedia*, pp. 5566–5574, 2024c.

Gao, H., Zhang, Y., Yang, J., and Dang, D. Mixed hierarchy network for image restoration. *Pattern Recognition*, 161: 111313, 2025.

Gu, Y., Meng, Y., Ji, J., and Sun, X. Acl: Activating capability of linear attention for image restoration. In *Proceedings of the Computer Vision and Pattern Recognition Conference*, pp. 17913–17923, 2025.

Guo, H., Li, J., Dai, T., Ouyang, Z., Ren, X., and Xia, S.-T. Mambair: A simple baseline for image restoration with state-space model. In *European Conference on Computer Vision*, pp. 222–241, 2024.

Guo, H., Guo, Y., Zha, Y., Zhang, Y., Li, W., Dai, T., Xia, S.-T., and Li, Y. Mambairv2: Attentive state space restoration. In *Proceedings of the Computer Vision and Pattern Recognition Conference*, pp. 28124–28133, 2025a.

Guo, Q., Li, X., Juefei-Xu, F., Yu, H., Liu, Y., and Wang, S. Jpgnet: Joint predictive filtering and generative network for image inpainting. In *Proceedings of the 29th ACM International conference on multimedia*, pp. 386–394, 2021.

Guo, Q., Qi, H., Sun, J., Juefei-Xu, F., Ma, L., Lin, D., Feng, W., and Wang, S. Efficientderain+: Learning uncertainty-aware filtering via rainmix augmentation for high-efficiency deraining. *International Journal of Computer Vision*, 133(4):2111–2135, 2025b.

Guo, Q., Wang, Z., Wang, L., Dong, H., Juefei-Xu, F., Lin, D., Ma, L., Feng, W., and Liu, Y. Carvenet: Carving point-block for complex 3d shape completion. *IEEE Transactions on Multimedia*, 27:1047–1058, 2025c.

Guo, X., Wang, X., Fu, X., and Zha, Z.-J. Deep unfolding network for image desnowing with snow shape prior. *IEEE Transactions on Circuits and Systems for Video Technology*, 35(5):4740–4752, 2025d.

He, K., Sun, J., and Tang, X. Single image haze removal using dark channel prior. *TPAMI*, 2011.

Jiang, K., Wang, Z., Yi, P., Chen, C., Huang, B., Luo, Y., Ma, J., and Jiang, J. Multi-scale progressive fusion network for single image deraining. *CVPR*, 2020.

Jiang, Y., Zhang, Z., Xue, T., and Gu, J. Autodir: Automatic all-in-one image restoration with latent diffusion. In *Computer Vision – ECCV 2024: 18th European Conference, Milan, Italy, September 29–October 4, 2024, Proceedings, Part XL*, pp. 340–359, 2024.

Kingma, D. and Ba, J. Adam: A method for stochastic optimization. *Computer Science*, 2014.

Kundur, D. and Hatzinakos, D. A novel blind deconvolution scheme for image restoration using recursive filtering. *IEEE Transactions on Signal Processing*, 46(2):375–390, 1998.

Li, B., Ren, W., Fu, D., Tao, D., Feng, D., Zeng, W., and Wang, Z. Benchmarking single-image dehazing and beyond. *TIP*, 28(1):492–505, 2018.

Li, Y., Tan, R. T., Guo, X., Lu, J., and Brown, M. S. Rain streak removal using layer priors. In *2016 IEEE Conference on Computer Vision and Pattern Recognition (CVPR)*, pp. 2736–2744, 2016. doi: 10.1109/CVPR.2016.299.

Liu, H., Liu, C., Xu, J., Jiang, P., and Lu, M. Xyscanet: An interpretable state space model for perceptual image deblurring. In *Proceedings of the Computer Vision and Pattern Recognition Conference (CVPR)*, pp. 779–789, 2025.

Liu, Y.-F., Jaw, D.-W., Huang, S.-C., and Hwang, J.-N. Desnownet: Context-aware deep network for snow removal. *IEEE Transactions on Image Processing*, 27(6):3064–3073, 2018. doi: 10.1109/TIP.2018.2806202.

Loshchilov, I. and Hutter, F. Sgdr: Stochastic gradient descent with warm restarts. 2016.

Luo, W., Qin, H., Chen, Z., Wang, L., Zheng, D., Li, Y., Liu, Y., Li, B., and Hu, W. Visual-instructed degradation diffusion for all-in-one image restoration. In *Proceedings of the IEEE/CVF Conference on Computer Vision and Pattern Recognition (CVPR)*, pp. 12764–12777, June 2025.

Mao, X., Li, Q., and Wang, Y. Adarevd: Adaptive patch exiting reversible decoder pushes the limit of image deblurring. In *2024 IEEE/CVF Conference on Computer Vision and Pattern Recognition (CVPR)*, pp. 25681–25690, 2024.

Mildenhall, B., Barron, J. T., Chen, J., Sharlet, D., Ng, R., and Carroll, R. Burst denoising with kernel prediction networks. In *Proceedings of the IEEE conference on computer vision and pattern recognition*, pp. 2502–2510, 2018.

Potlapalli, V., Zamir, S. W., Khan, S., and Khan, F. S. Promptir: Prompting for all-in-one blind image restoration. *Advances in Neural Information Processing Systems (NeurIPS)*, 2023.

Rong, J., Huang, H., and Li, J. Imu-assisted accurate blur kernel re-estimation in non-uniform camera shake deblurring. *IEEE Transactions on Image Processing*, 33: 3823–3838, 2024.

Su, X., Li, S., Cui, Y., Cao, M., Zhang, Y., Chen, Z., Wu, Z., Wang, Z., Zhang, Y., and Yuan, X. Prior-guided hierarchical harmonization network for efficient image dehazing. In *Proceedings of the AAAI Conference on Artificial Intelligence*, volume 39, pp. 7042–7050, 2025.

Wang, C., Pan, J., Wang, L., and Wang, W. Intra and inter parser-prompted transformers for effective image restoration. In *Proceedings of the AAAI Conference on Artificial Intelligence*, volume 39, pp. 7609–7618, 2025.

Wen, Y., Gao, T., and Chen, T. Unpaired photo-realistic image deraining with energy-informed diffusion model. In *Proceedings of the 32nd ACM International Conference on Multimedia*, pp. 360–369, 2024.

Yang, W., Tan, R. T., Feng, J., Liu, J., Guo, Z., and Yan, S. Deep joint rain detection and removal from a single image. *CVPR*, pp. 1685–1694, 2016.

Yao, M., Xu, R., Guan, Y., Huang, J., and Xiong, Z. Neural degradation representation learning for all-in-one image restoration. *IEEE Transactions on Image Processing*, 33: 5408–5423, 2024.

Zamir, S. W., Arora, A., Khan, S., Hayat, M., Khan, F. S., Yang, M.-H., and Shao, L. Multi-stage progressive image restoration. In *CVPR*, 2021.

Zeng, H., Cao, J., Zhang, K., Chen, Y., Luong, H., and Philips, W. Unmixing diffusion for self-supervised hyperspectral image denoising. In *2024 IEEE/CVF Conference on Computer Vision and Pattern Recognition (CVPR)*, pp. 27820–27830, 2024.

Zeng, H., Wang, X., Chen, Y., Su, J., and Liu, J. Vision-language gradient descent-driven all-in-one deep unfolding networks. In *Proceedings of the IEEE/CVF Conference on Computer Vision and Pattern Recognition (CVPR)*, pp. 7524–7533, June 2025.

Zhang, H. and Patel, V. M. Density-aware single image de-raining using a multi-stream dense network. *CVPR*, pp. 695–704, 2018.

Zhang, H., Sindagi, V. A., and Patel, V. M. Image de-raining using a conditional generative adversarial network. *TCSVT*, 30:3943–3956, 2017.

Zhang, M. and Gunturk, B. K. Multiresolution bilateral filtering for image denoising. *IEEE Transactions on Image Processing*, 17(12):2324–2333, 2008.

Zhang, X., Ma, J., Wang, G., Zhang, Q., Zhang, H., and Zhang, L. Perceive-ir: Learning to perceive degradation better for all-in-one image restoration. *IEEE Transactions on Image Processing*, pp. 1–1, 2025.

A. Loss Function

Consistent with prior work, we optimize OPIR jointly in the spatial and frequency domains. The overall objective function is formulated as:

$$\begin{aligned}
 L &= \sum_{i=1}^3 (L_c(\hat{J}_i, \bar{I}) + \delta L_e(\hat{J}_i, \bar{I}) \\
 &\quad + \lambda L_f(\hat{J}_i, \bar{I})) \\
 L_c &= \sqrt{\|\hat{J}_i - \bar{I}\|^2 + \epsilon^2} \\
 L_e &= \sqrt{\|\Delta \hat{J}_i - \Delta \bar{I}\|^2 + \epsilon^2} \\
 L_f &= \|\mathcal{F}(\hat{J}_i) - \mathcal{F}(\bar{I})\|_1
 \end{aligned} \tag{22}$$

where i indexes the input–output image pairs, and \bar{I}_i denotes the corresponding ground-truth images. \mathcal{L}_c is the Charbonnier loss, with the constant ϵ empirically set to 0.001 in all experiments. \mathcal{L}_e is an edge-aware loss, where Δ denotes the Laplacian operator, encouraging accurate reconstruction of high-frequency structures. \mathcal{L}_f represents the frequency-domain loss, in which $\mathcal{F}(\cdot)$ denotes the fast Fourier transform. The weighting factors λ and δ are set to 0.1 and 0.05, respectively, following (Zamir et al., 2021; Cui et al., 2023a).

B. More Experiments

B.1. Experimental Setup

Datasets. For the task-aligned setting, we train the deraining model using 13,712 paired clean–rain images collected from multiple datasets (Yang et al., 2016; Zhang et al., 2017; Fu et al., 2017; Li et al., 2016). The trained OPIR is evaluated on several benchmark test sets, including Rain100H (Yang et al., 2016), Rain100L (Yang et al., 2016), Test100 (Zhang et al., 2017), and Test1200 (Zhang & Patel, 2018). For desnowing evaluation, we adopt the Snow100K (Liu et al., 2018), SRRS (Chen et al., 2020), and CSD (Chen et al., 2021) datasets. To ensure consistency with the training strategy of previous work (Cui et al., 2023a), we randomly sample 2,500 image pairs for training and 2,000 images for evaluation. For dehazing, we assess the performance of our OPIR on daytime synthetic datasets from RESIDE (Li et al., 2018), which include the indoor training set (ITS), the outdoor training set (OTS), and the synthetic objective testing set (SOTS). The model is trained separately on ITS and OTS, and then evaluated on the corresponding SOTS-Indoor and SOTS-Outdoor test sets, each containing 500 paired images.

For the all-in-one setting, we combine the above image restoration datasets to construct a unified training set. During evaluation, we use Test100 (Zhang et al., 2017) for deraining, Snow100K (Liu et al., 2018) for desnowing, and SOTS-Outdoor (Li et al., 2018) for dehazing.

Training details. All models are optimized using the Adam optimizer (Kingma & Ba, 2014) with $\beta_1 = 0.9$ and $\beta_2 = 0.999$. The learning rate is initialized at 2×10^{-4} and progressively reduced to 1×10^{-7} according to a cosine annealing strategy (Loshchilov & Hutter, 2016). During training, we randomly crop 256×256 patches with a batch size of 32 and train the models for 4×10^5 iterations. Horizontal and vertical flipping are applied for data augmentation. To ensure fair comparisons, all deep learning-based baselines are fine-tuned or retrained following the hyperparameter configurations reported in their original works.

B.2. EfDeRain+ (Guo et al., 2025b) vs. OPIR

EfDeRain+ (Guo et al., 2025b) tackles the limitations of naive cascaded predictive filtering by introducing an uncertainty map derived from the statistics of predicted kernels, which enables a second-stage refinement that focuses on regions that are difficult to reconstruct. While this strategy is effective for single-task deraining, it remains inherently task-specific. Both predictive networks are trained exclusively for rain removal, and the uncertainty formulation is based on assumptions about kernel weight distributions that are closely coupled with rain streak characteristics. Consequently, extending EfDeRain+ (Guo et al., 2025b) to other restoration tasks requires retraining separate models, which restricts its general applicability.

In contrast, OPIR reformulates cascaded predictive filtering as a unified inverse operator learning framework rather than a task-dependent refinement scheme. Instead of learning independent predictive filters for different degradations, OPIR

models a shared base inverse operator that is explicitly modulated by a task-aware module. Task information is injected directly at the operator level through lightweight, task-conditioned modulation, allowing a single backbone network to adapt its inverse behavior across heterogeneous restoration tasks. This design enables OPIR to capture degradation-specific characteristics while maintaining parameter efficiency and strong cross-task generalization.

A further distinction lies in uncertainty modeling. EfDeRain+ (Guo et al., 2025b) estimates uncertainty by averaging predicted kernel weights, motivated by the observation that rain-corrupted pixels often exhibit characteristic positive–negative weight patterns. Although effective for deraining, this formulation implicitly depends on task-specific kernel distributions. In contrast, OPIR defines uncertainty directly from the magnitude of the predicted inverse operator, reflecting the strength of local dependencies required to reconstruct each pixel. This operator-centric uncertainty formulation is task-agnostic and characterizes reconstruction difficulty from a physical perspective, making it applicable to a broader range of degradations beyond rain.

The role of the two-stage design also differs fundamentally between the two methods. In EfDeRain+ (Guo et al., 2025b), cascaded filtering serves as a heuristic refinement step in which the second stage compensates for residual rain artifacts. In OPIR, the two stages correspond to progressive inverse operator estimation. The first stage produces an initial task-aware restoration together with an uncertainty map, while the second stage re-estimates the inverse operator conditioned on both the intermediate result and the uncertainty. This leads to a principled, uncertainty-guided operator refinement process rather than repeated filtering.

Finally, although both approaches employ weight-sharing multi-scale dilated filtering for computational efficiency, EfDeRain+ (Guo et al., 2025b) applies this strategy within a single-task deraining pipeline. OPIR integrates multi-scale filtering into a task-aware inverse operator framework, enabling adaptive receptive field selection at the pixel level while preserving low computational complexity. Moreover, OPIR generates offsets for all scales within a single loop, performs multi-scale convolution in parallel, and further reduces redundant computation through learnable fusion weights.

Table 7. Ablation study on EfDeRain+ (Guo et al., 2025b).

Method	PSNR	Δ PSNR
EfDeRain+ (Guo et al., 2025b)	31.46	-
add Task-aware module	33.11	+ 1.65 dB
replace with Multi-scale kernel	31.75	+ 0.29 dB
replace with Multi-scale kernel + Task-aware module	33.69	+ 2.23 dB

To further demonstrate the advantages of our approach, we adopt EfDeRain+ (Guo et al., 2025b) as the baseline and progressively replace or incorporate the modules proposed in this paper. This controlled modification strategy allows us to directly assess the effectiveness of each component.

Table 7 reports an ablation study based on EfDeRain+ (Guo et al., 2025b), analyzing the contributions of task-aware inverse operator modeling and multi-scale kernel design. Introducing the task-aware module alone leads to a substantial performance gain of +1.65 dB, which clearly surpasses the improvement obtained by replacing the single-scale kernel with a multi-scale kernel (+0.29 dB). This observation suggests that explicitly modulating the predicted inverse operator according to task characteristics plays a more crucial role than simply enlarging the receptive field. When both components are jointly applied, the proposed method achieves an overall improvement of +2.23 dB compared to the baseline.

B.3. Additional Visual Results

Figure 6 presents qualitative comparisons of our method under the all-in-one experimental setting, where a single unified model is used to handle multiple degradation types. Figure 7 shows the corresponding visual results under the task-aligned setting, in which the model is explicitly adapted to each specific degradation. As can be seen, our approach effectively removes diverse degradations across both settings, while consistently reconstructing images with sharp structural details, natural textures, and visually pleasing overall appearance. These results demonstrate the robustness and strong generalization capability of the proposed method under different restoration paradigms.

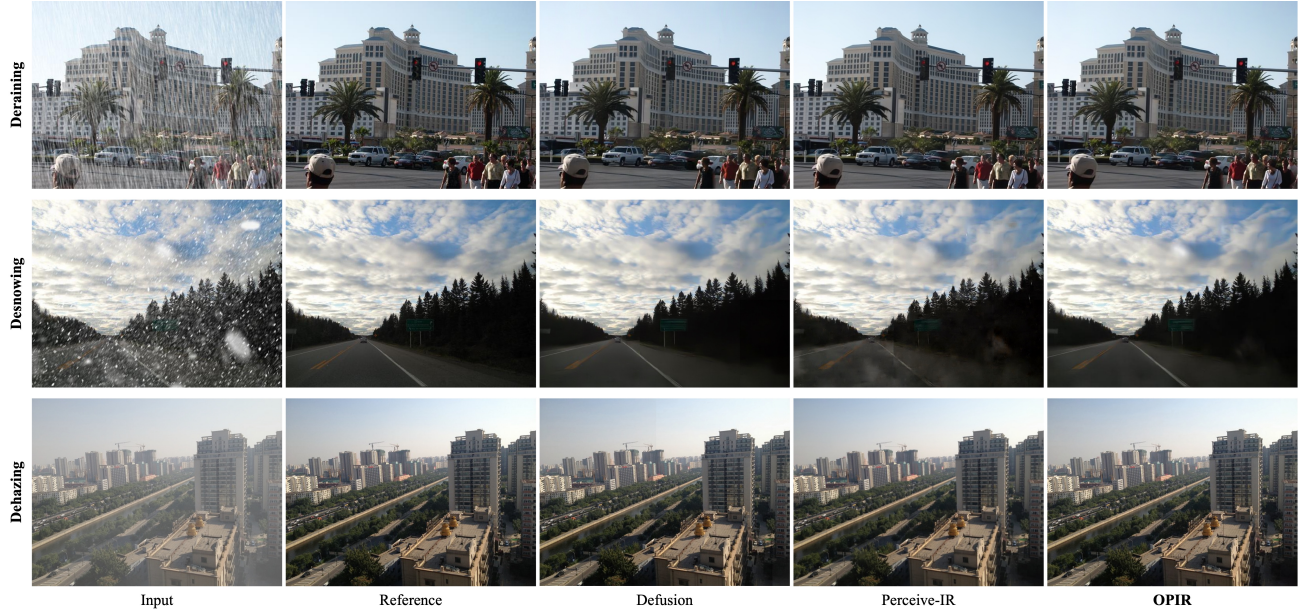


Figure 6. Qualitative results under the all-in-one experimental setup.



Figure 7. Qualitative results under the task-aligned experimental setup.